1   **An In-situ 3D Micro-XRD Investigation of Water Uptake by Alkali-Silica-Reaction**

2   **(ASR) Product**

3

4   Guoqing Geng [a,b,*], Solène Barbotin [c], Mahdieh Shakoorioskooie [d,e,f], Zhenguo Shi [d], Andreas

5   Leemann [d], Dario Ferreira Sanchez [g], Daniel Grolimund [g], Erich Wieland [b], Rainer Dähn [b].

6

7   [a] Department of Civil and Environmental Engineering, National University of Singapore,

8   117576 Singapore.

9   [b] Laboratory for Waste Management, Paul Scherrer Institute, 5232 Villigen PSI, Switzerland.

10   [c] Laboratory of Construction Materials, Swiss Federal Institute of Technology (EPFL),

11   Ecublens, 1015 Lausanne, Switzerland.

12   [d] Concrete and Asphalt Laboratory, Empa, Swiss Federal Laboratories for Materials Science

13   and Technology, CH-8600 Dübendorf, Switzerland

14   [e] Institute for Building Materials (IfB), ETH Zürich, Stefano-Franscini-Platz 3, CH-8093

15   Zürich, Switzerland

16   [f] Center for X-ray Analytics, Empa, Swiss Federal Laboratories for Materials Science and

17   Technology, CH-8600 Dübendorf, Switzerland

18   [g] Swiss Light Source, Paul Scherrer Institute, 5232 Villigen PSI, Switzerland

19   [*] Correspondence e-mail: ceegg@nus.edu.sg

20

21   **Abstract**

22   The ASR products in concrete have various chemical compositions. It is yet unclear whether

23   and how these products develop micro-expansion upon moisture ingress. This paper presents a

24   3D in-situ observation of the crystallography and volume change of an ASR-product-filled vein,

25   under varying relative-humidity (R.H.). The vein was observed to contain two nano-crystalline

phases with distinct basal spacings, and distribute heterogeneously in space. When R.H. changed from 10% to >38%, the basal spacing increased from 7.43Å to 8.89Å for one phase, whereas remained constant (~10.9Å) for the other. This is the first time that an ASR product is observed in-situ to exhibit crystal structural expansion during wetting process. However, the product-filled vein exhibited no noticeable swelling when R.H. varied from 10% to 97%. Our findings provide the first direct evidence that the moisturization-induced crystal structural change of ASR product may not be a plausible explanation to the macroscale concrete expansion.

1. Introduction

Alkali-Silica-Reaction (ASR) is a commonly known mechanism of concrete degradation, but its microscale origin is not widely known. This ASR products cause expansion in concrete in the presence of moisture, leading to crack formation and concrete degradation [1,2]. ASR-induced deterioration has been reported worldwide, and a global effort of investigating ASR exists since the mid-20th century [3,4]. Today, multiple standard testing methods have been established to evaluate the ASR reactivity of aggregates [5,6]. Limiting the alkali content of cement is also incorporated in construction codes to minimize the long-term ASR risk [7]. These measures are vastly helpful in construction practice, yet different testing methods may sometimes provide controversial results, and fail to predict the premature ASR degradation [8,9]. Meanwhile, computational simulations of ASR-induced material degradation are frequently reported over the past 20 years [10-12]. Many of them are based on conceptual

50 mechanisms that lack microscale validation. There is thus an urgent need to deepen our

51 understanding to the microscale mechanism of the ASR process.

52 One of the most widely accepted hypotheses of ASR damage is the moisture-driven swelling

53 [13-15] of the products which bear a general composition of sodium/potassium calcium silicate

54 hydrates. Compared with the calcium silicate hydrate (C-S-H, the main hydration product in

55 Portland cement concrete), the ASR gel has a much higher content of Na+K and a much lower

56 content of Ca [15-18]. This compositional difference results in a higher degree of silicate

57 polymerization in the ASR product (Q^3 dominant) than in C-S-H (Q^1/Q^2 dominant) [16,19]. It

58 is proposed that ASR product expands upon up-taking water to its gel structure, leading to a

59 local stress development and initiation of cracks in concrete [13-15]. This hypothesis has been

60 challenged recently at least by two research evidences. First, large amount of SEM data have

61 indicated that the ASR product inside the reacted aggregates often exhibit a nano-crystalline

62 nature. The product vein is a 'river' of nano-platelets that are tens of nanometers thick and

63 micron-size wide [20-22]. These products are distinct from a gel-appearance, and their time-

64 dependent mechanical property is yet to be justified [22,23].

65 Second, recent micro-XRD and micro-spectroscopic evidences have unveiled the high

66 similarity between the nano-crystalline ASR product and shlykovite – a layer-silicate mineral

67 [16,17,24-27]. They were both reproduced in recent laboratory synthesis attempts. Although

68 multiple basal spacing values were found for ASR products from the field and lab-synthesis

69 [31], it was noted that they all seem not able to swell or shrink upon a significant R.H. change

70 [19, 26, 28]. Temperature is found to affect the formation of different types of crystalline ASR

71 products with varying basal spacing, i.e., 12.0 Å (<40 °C), 10.8 Å (around 40 °C), and 13.1 Å

72 (60–80 °C for K-shlykovite) [26,29,30]. Moreover, a significant hydrostatic compression

73 pressure (>2 GPa) can also alter the basal spacing [31]. These evidences make it questionable

74 whether moisture-induced swelling is the microscale source of expansive stress during the ASR

75 damage.

76 To answer this question, a microscale in-situ observation of a vein filled with the ASR product

77 and subject to R.H. change would provide unparalleled evidence. This paper reports exactly an

78 approach of such kind. A vein filled with crystalline ASR product was carefully isolated from

79 a degraded concrete and then investigated by synchrotron-based micro-XRD. The sample was

80 exposed to an inert atmosphere (N_2) with a largely varying R.H. (10%, 38% and 97%). The

81 combined use of micro-XRD and tomographic scanning allows reconstructing the XRD pattern

82 of each voxel in the probed volume, which then enables monitoring the crystal structure of the

83 product during the R.H. variation, along with its volumetric change (if any). The results provide

84 a direct evidence of whether the crystalline ASR product undergoes a structural swelling upon

85 contacting moisture, and whether this leads to a volumetric change inside the product vein.

86

87 **2. Methodology**

88 **2.1 Materials**

89 The ASR product was extracted from a laboratory-produced concrete cube exposed for 14 years

90 to natural conditions in Valencia (Spain), with noticeable ASR degradation. The reactive

91 aggregate is a silicified limestone [32]. This concrete was referred to as 'ES1' in our previous

92 studies [24,31]. An iron hammer was used to gently crush the concrete. Via inspection under a

93 stereoscopic optical microscope, a fragment with abundant ASR product veins on the fractural

94 surface was selected. No resin impregnation was applied to the sample. A scanning electron

95 microscope (Quanta 200 ESEM, FEI) at a pressure of $1.0\text{-}2.0 \times 10^{-5}$ mbar, an accelerating

96 voltage of 15kV and a beam current of 95-100 µA was used to locate the region of interest. An

97 SSD detector (30 mm^2) from Bruker and Esprit energy software with PhiRhoZ quantification

98 were operated for the Energy-dispersive X-ray spectroscopy (EDS) analysis.

99 The region of interest was extracted with a plasma focused ion beam (Helios G4 PFIB

100 DualBeam UXe, ThermoFischer Scientific). A ~50 μm wide product vein was spotted on the

101 fractural surface. An SEM-EDS line-scan perpendicular to the vein (containing 24 points from

102 the edge to the middle of the vein) indicated an average $(Na+K)/Si=0.40$ and $Ca/Si=0.32$. This

103 product vein was then cut with the Xenon plasma ion beam at working currents ranging from

104 2μA down to 0.2μA. The extracted volume was a cuboid with edge lengths of 40-80 μm,

105 containing part of an ASR product vein embedded in an aggregate (limestone) matrix (Figure

106 1a). It was then fixated to the tip of an aluminum pin using Pt as the welding material. A second

107 step to clean the sample was operated in a focused ion beam (FIB, NVision 40 CrossBeam,

108 Zeiss), at much lower currents ranging from 65nA to 27nA, with Gallium ion beam. The sample

109 was then placed in a desiccator containing saturated NaOH solution as CO_2 and moisture trap,

110 until it was measured two days later.
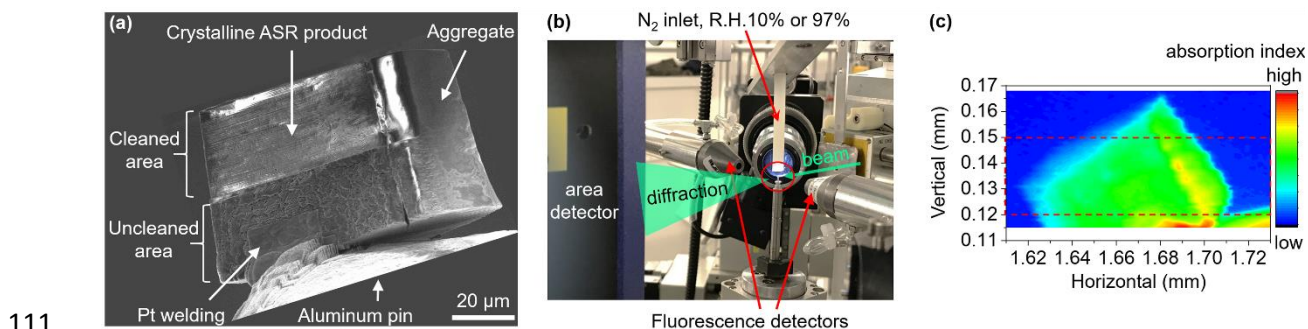
111

112 Figure 1. Overview of the sample and the beamline setup. (a) SEM image of the extracted

113 volume. The surface was partly cleaned with FIB to expose the morphogen of the ASR product.

114 (b) Sample placed on the sample stage between the beam upstream, XRD and fluorescence

115 detectors, with a N_2 flow approaching from top; (c) An absorption contrast image of the sample

116 during the scanning, viewed from an angle slightly different from (a).

117

118 **2.2 micro-XRD tomography**

119 The micro-XRD measurement was performed at the microXAS beamline of the Swiss Light

120 Source (SLS) [33]. An incident beam of 14.6 keV energy was focused to ~ 1 μm × 1 μm using

121 Kirkpatrick-Baez mirrors. As shown in Figure 1b, an Eiger4M area detector was used to record

5

122　the diffraction pattern of the scanned region on the sample. The sample-to-plate distance and

123　the position of the beam center were calibrated using the diffraction pattern of a standard

124　material (LaB_6). A pair of fluorescence detectors were placed in equal distance on both sides

125　of the sample with respect of the beam direction. The elemental concertation in the scanned

126　region were semi-quantified by averaging the signals from both fluorescence detectors, which

127　is used to differentiate the ASR product from other phases. Reconstructions were conducted

128　using the selected florescence signal with home-made python codes and the Astra Toolbox

129　library, using SIRT method and parallel beam GPU code [34,35].

130　Using x-ray absorption contrast imaging, the sample was readily located during the scanning

131　(Figure 1c). The raw XRD pattern contained the information of all materials along the beam

132　path. Hence, a tomographic scanning manner was adopted to decouple the diffraction

133　contributed by different parts of the sample. At each height (vertical position), horizontal

134　scanning at a step size of 1 µm was combined with a rotational scanning at a step size of ~1.6°,

135　covering an angle range of ~180°. The scanning of each slice took ~65 min. Such tomographic

136　scans were conducted on multiple slices along the vertical direction. The overall investigated

137　region is indicated by the red-dashed rectangle in Figure 1c.

138　To study the effect of R.H., the sample was blown from top using either pure (dry) N_2 or N_2

139　that passed through a water reservoir. The R.H. was measured as 10% (dry N_2) and 97% (water-

140　saturated N_2), hereafter denoted as '*dry*' and '*wet*' conditions, respectively. For each R.H.

141　condition, 21 consecutive slices were scanned. The step size between adjacent slices is 1.5 µm

142　for the dry condition, and 1.2 µm for the wet condition (vertical position of each scanned slices

143　available later in Figure 5). The N_2 blow was lastly removed to study the sample at ambient

144　R.H., which was measured to be 38% in the experiment hutch, hereafter denoted as '*amb*'

145　condition. Due to the limitation of experiment time, only four slices were studied at the ambient

146   condition. The measurement starts from *dry*, followed by *wet* and *amb* conditions. The sample

147   was allowed one-hour equilibration each time after a R.H. change.

148   For the tomographic scan of each slice, one XRD pattern was collected for each horizontal

149   position at each rotation angle. A set of home-made codes were used to translate these

150   diffraction patterns to a diffractogram of intensity *vs* 2theta [36, 37]. Matlab software was then

151   used to reconstruct the slice using the diffraction intensity at each 2theta angle as the contrast.

152   For each slice, this reconstruction resulted in a three dimensional data, with the first and second

153   dimensions corresponding to the x- and y- coordinates of the pixels on the slice, the third

154   dimension corresponding to the 2theta angle. This eventually yielded the XRD pattern of each

155   point in the studied volume under various R.H. conditions. Spatial distribution of a certain

156   phase on each slice was obtained through reconstruction using the integrated intensity of its

157   characteristic XRD peaks (e.g. the basal peak) using a python code of simultaneous iterations

158   reconstruction technique (SIRT) algorithm [34,35]. Open source packages *ImageJ* [38] and

159   *Paraview* [39] were used for visualization.

160

161   **3. Results and discussions**

162   **3.1 micro-XRD of the ASR products**

163   A projection of the sample is shown with Ca, absorption and Pt contrast (Figure 2a). In the Ca

164   contrast image, the regions containing relatively high and low Ca content correspond to the

165   calcite aggregate and the ASR product, respectively. The deposited Pt weld is clearly resolved

166   on the surface of the sample. To analyze the influence of R.H. change to the crystal structure

167   of the ASR product, three slices at different vertical positions were selected (Figure 2a). For

168   each slice, the XRD at all horizontal positions and all rotational angles were summed as the

169   overall XRD of this slice, denoted as *dry/wet/amb*_slice1/2/3 as shown in Figure 2b. Only

170   slice3 was studied at *amb* condition due to limited synchrotron beamline time.

171 Under a certain R.H. condition, the diffraction patterns of ASR products were comparable

172 among different slices (Figure 2b). The peak intensities of slice1 were weaker than those of

173 slice2 and slice3, since there was less solid material in slice1. The XRD of each slice typically

174 contained the contribution from the ASR products, and from calcite (aggregate) and Pt as

175 labelled in Figure 2b. Although not displayed in Figure 2, this finding holds true for all the

176 scanned slices under a certain R.H., demonstrating that the crystal composition is comparable

177 among different slices.

178 Two basal peaks were observed at $d \sim 10.9$ Å and 7.43 Å when the sample is dry (R.H.=10%).

179 Upon increasing R.H. to 97%, the 7.43 Å basal peak vanished while a new basal peak appeared

180 at $d \sim 8.89$ Å. The 10.9 Å basal peak remained unchanged. Meanwhile, two new peaks appeared

181 in the wet condition at 2theta of ~15° and ~25° (red arrows in Figure 2b). The peak at 29.5°

182 were sharper and more intensive in the wet condition as compared with the dry condition. When

183 R.H. subsequently dropped from 97% to 38% (*amb*), no noticeable change of the XRD was

184 observed after 5 hours of equilibration and measurement.

185
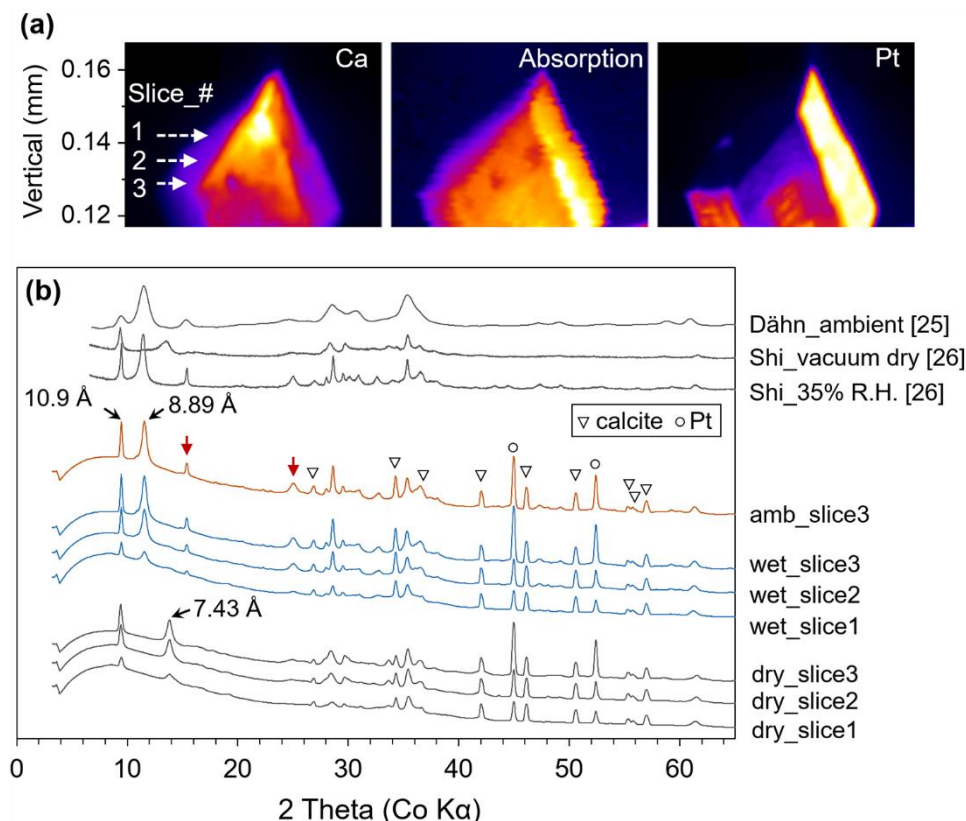
Figure 2. XRD data of the ASR products under different R.H. (10% for dry, 97% for wet and 38% for ambient). (a) Projections of the sample in Ca, absorption and Pt contrast, with the vertical positions of three selected slices labeled. (b) The XRD of the selected slices plotted together with reported data [25,26]. Diffraction peaks not from ASR are labeled with triangle (calcite) and circle (Pt). The 2theta angle of synchrotron beam was translated to the equivalent Co Kα value, according to the Bragg equation.

The basal spacing of the crystalline ASR product is found to be highly variable. In our previous work, ASR products exhibited similar layer structure as shlykovite, but with various basal peaks at $d \sim$ 8.6, 9.6, 10.6, 12.2 and 13.4 Å [24,25,31]. For samples from different field sources, the dominant peak in all cases appears to be at $d \sim$ 12.2 Å [24]. For lab synthesized shlykovite-type ASR samples at elevated temperature (e.g. 60 °C and 80 °C), a basal spacing larger than 13 Å was often observed [17,19]. When the synthesis temperature dropped to 40 °C, a product with basal peaks at 10.8 Å and 8.9 Å was reported [26]. These two basal spacings remained unchanged when R.H. was reduced to 35% (Figure 2b Shi_35% R.H.), yet a clear change took place when the sample was vacuum-dried for three days (Figure 2b Shi_vacuum dry) [26]. It is clearly shown in Figure 2b that the XRD of the 40 °C-synthesized sample are highly comparable to the results in this study. A previously reported micro-XRD data (Figure 2b Dähn_ambient) also resembles the results in this study at *wet* and *amb* condition, while the ~8.9 Å peak is much more dominant in the reported work [25].

In the reported lab-synthesis work [26], SEM observation and spectroscopic data indicated that the obtained ASR product seems to have a uniform morphology and chemical environment. However, the variation in the intensity ratio between the 10.9 Å and 8.89 Å (7.43 Å) peak and their distinct response to R.H.-change indicate that they might come from two crystalline phases with similar layer structure but different basal spacings.

3.2 Tomographic reconstruction

To further investigate the source of the two basal peaks, the azimuthally integrated intensity was used to retrieve the spatial distribution of phases that produce them (hereafter denoted as phase basal_1 and basal_2, respectively). With the scanning tomographic X-ray powder diffraction technique, every voxel in the scanned volume should satisfy a powder diffraction condition [40]. The ASR products are nano-platelets with thickness of tens-of-nm, which is much smaller than the pixel size (1 µm × 1 µm). As shown by a raw pattern example (inset in Figure 3a), the diffraction rings of basal peak 10.9 Å (basal_1) and 7.43 Å (basal_2) are both continuous rings with approximately homogeneous distribution of intensity at all azimuthal angles, i.e. satisfying the powder diffraction condition. Meanwhile, this diffraction contrast reconstruction cannot be applied to the aggregate since it exhibited a strongly spotty diffraction from large single-crystal calcite grains. As such, the whole scanned volume was reconstructed using the Ca fluorescence contrast, and segmented to ASR product and aggregate, i.e. the grey and orange volume in Figure 3a (partially transparent for viewing convenience).
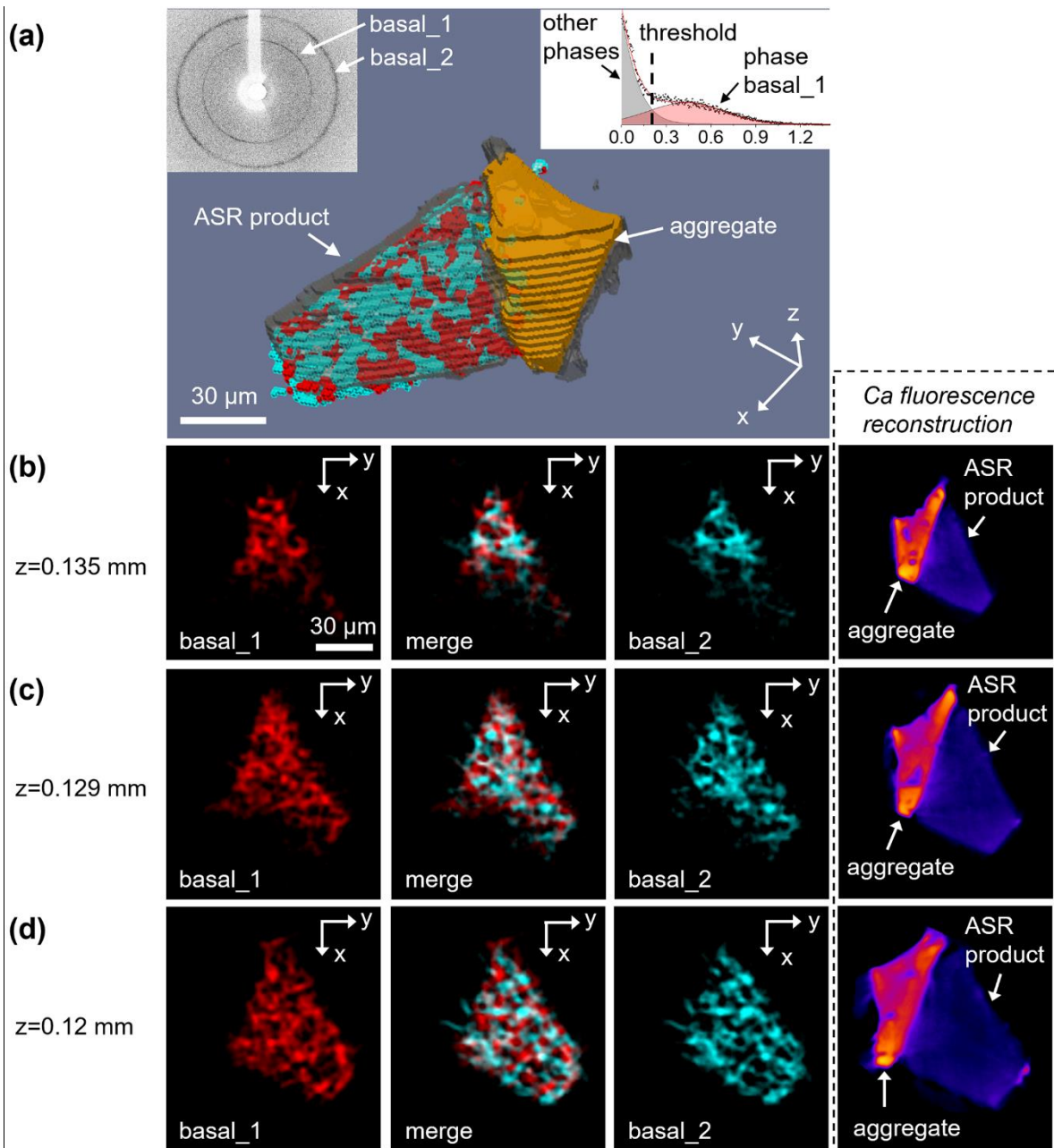
Figure 3. Reconstructed spatial distribution of phases (in dry condition) that produce basal peaks 10.9 Å (basal_1, red) and 7.43 Å (basal_2, cyan). (a) Volume rendering of the ASR product (red and cyan) inside the whole scanned volume (reconstructed using Ca contrast). (b-d) Compared distribution of the phases basal_1 and basal_2 in three selected slices. A grey color in the merged image indicates the co-existence of both phases. The corresponding slices reconstructed with Ca Kα fluorescence signal are also display for comparison. Images reconstructed from diffraction contrast are binary-segmented.

A threshold-segmentation was applied to the ASR phases reconstructed with their basal peak diffraction contrast, which is well differentiated from other phases. An example of the basal_1

11

237   diffraction contrast histogram is shown by the inset in Figure 3a (right-hand-side). Inside the

238   scanned volume, the basal_1 phase (red) and basal_2 phase (cyan) are intermixed in a sub-

239   volume that is consistent with the location of the ASR product (Figure 1a). The distribution of

240   basal_1 and basal_2 phases are further illustrated in three selected slices, together with slices

241   reconstructed using Ca fluorescence signal (Figure 3b-d). The Ca contrast images demonstrate

242   two regions with distinct Ca content, corresponding to aggregate (left) and ASR product (right).

243   In each slice, both basal_1 and basal_2 phases spread within the region corresponding to the

244   ASR product. The distribution of each phase, however, is not homogeneous. There are regions

245   rich in a single phase, while between them are regions with no diffraction signal of this phase.

246   When merging the distribution of basal_1 and basal_2, the vacancies in the distribution of one

247   phase often host the other phase, though some regions seem to contain both phases (grey color

248   region in Figure 3b-d). This suggests the ASR products that produce the peak 10.9 Å (basal_1)

249   and peak 7.43 Å (basal_2) are not the same. At the micron-scale, they are distributed differently

250   inside an ASR product vein. Meanwhile, the distribution of Ca does not exhibit a similar

251   heterogeneity as the distribution of basal_1 and basal_2, indicating that the two phases share

252   similar content of Ca.

253   The diffraction-contrast reconstruction was applied also to the data in *wet* (97% R.H.) and *amb*

254   (38% R.H.) conditions. For comparison, the reconstructed images of a slice at the vertical

255   position of 0.130 ± 0.0005 mm are plotted together (Figure 4). The distribution of phase basal_1

256   in *dry*, *wet* and *amb* conditions are colored in red, green and blue, respectively (Figure 4a). A

257   slight change in the measured vertical position in different R.H. conditions results in a few

258   local variations in the distribution of basal_1. Apart from that, the overall size of the distributed

259   area of phase basal_1 remains vastly unchanged, as indicated by the yellow dashed lines in

260   Figure 4a.
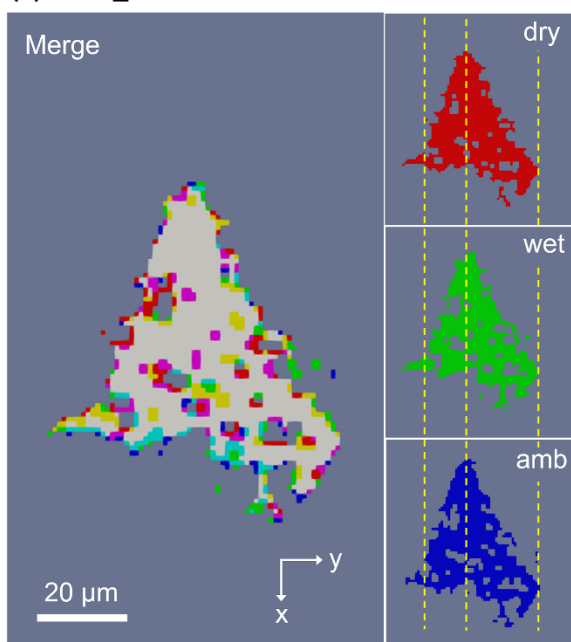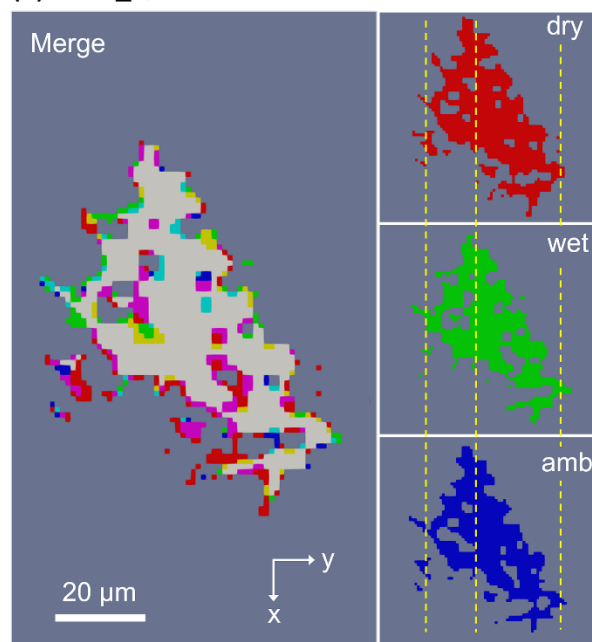
Figure 4. Comparison of the micro-distribution of (a) phase basal_1 and (b) basal_2 under varying R.H. conditions. The yellow dashed lines are eye-guides of the size of the distributed area. Red, green and blue are used for the *dry*, *wet* and *amb* conditions, respectively. In the merged image, binary overlaps are represented by purple (red & blue), yellow (red & green) and cyan (blue & green). The grey area indicates an overlap of three basic colors.

The distribution of basal_2 in the *wet* and *amb* conditions were reconstructed using the intensity of the 8.89 Å peak, in comparison to the 7.43 Å peak in dry condition. As shown in Figure 4b, the nearly identical distribution of basal_2 in all three R.H. conditions readily suggests that it is the same phase that produces peak 7.43 Å when dry and peak 8.89 Å when wet. In other words, the phase basal_2 has undergone an enlargement of basal spacing when R.H. increased from 10% to >38%. This is the first time that a microscale ASR product has been observed to exhibit crystal structural expansion in an in-situ wetting process. Yet surprisingly, the spatial distribution of basal_2 exhibits nearly zero change during the wetting process, although the basal peak shift corresponds to a ~20% volume increase of the crystal structure. Otherwise stated, the crystal structural swelling of the ASR product basal_2 did not lead to a swelling of the product vein at microscale (Figure 4b).

279   The threshold segmentation was applied to all the reconstructed slices in different R.H.

280   conditions. The volume (number of voxels) of phase basal_1 and basal_2 were counted and

281   plotted as a function of the vertical positions, as shown in Figure 5a and 5b. For all slices, there

282   is no clear change in volume for both basal_1 and basal_2 phases in all studied R.H. conditions.

283   Their volume ratio at each vertical position is also consistent throughout R.H. change (Figure

284   5c). These data again suggest that the microscale volume of the ASR product remains

285   unchanged during R.H. variation, despite the change of their crystal structure size.
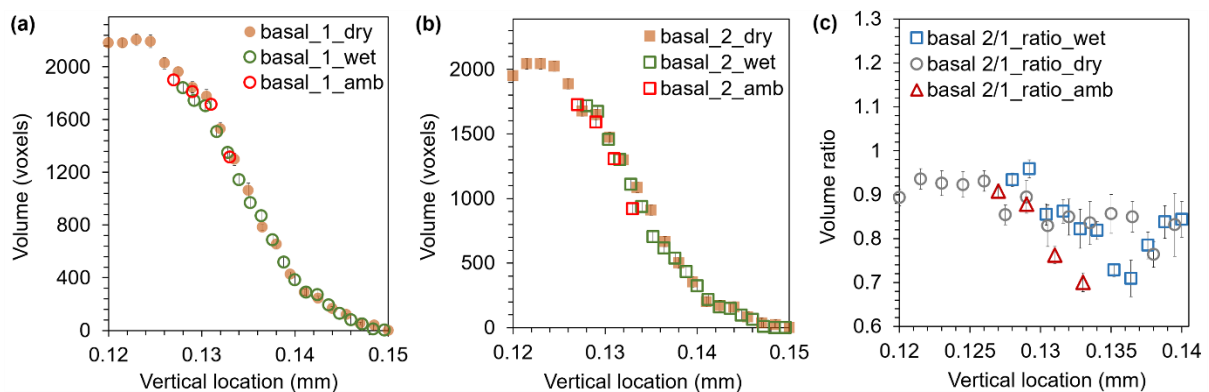

287   Figure 5. Reconstructed volume (number of voxels) of phase basal_1 (a), basal_2 (b) and their
288   ratios as a function of the vertical position in various R.H. conditions. The uncertainty is
289   indicated by the error bar, which is estimated by varying the segmentation threshold value by
290   ±5%. The volume ratio in (c) does not include slices with vertical location higher than 0.14
291   mm, since the volume is too small and the error bar thus too large.

292

293   **3.3 Implications on moisture uptake by ASR product**

294   The reconstructed 3D XRD data enables the diffractogram to be extracted from voxels that

295   contain only phase basal_1 or basal_2, as shown in Figure 6a. The strong orientations of Pt and

296   calcite have resulted in significant reconstruction artifacts in the XRD patterns. Therefore the

297   2theta ranges corresponding to calcite and Pt diffractions are masked in Figure 6a for viewing

298   convenience. For phase basal_1, its diffractogram in wet and dry condition were mostly

299   comparable. The 2theta positions of all diffraction peaks remained unchanged. Meanwhile, the

300   (100) and (106) peaks were much sharper when basal_1 is wet, suggesting that the drying has

14

resulted in a certain degree of amorphousness. For phase basal_2, the basal peak drifted significantly when R.H. changes from 10% to above 38%. A loss of crystallinity was also observed when phase basal_2 is dry, as indicated by the broadening of several sharp peaks that were present in wet condition.
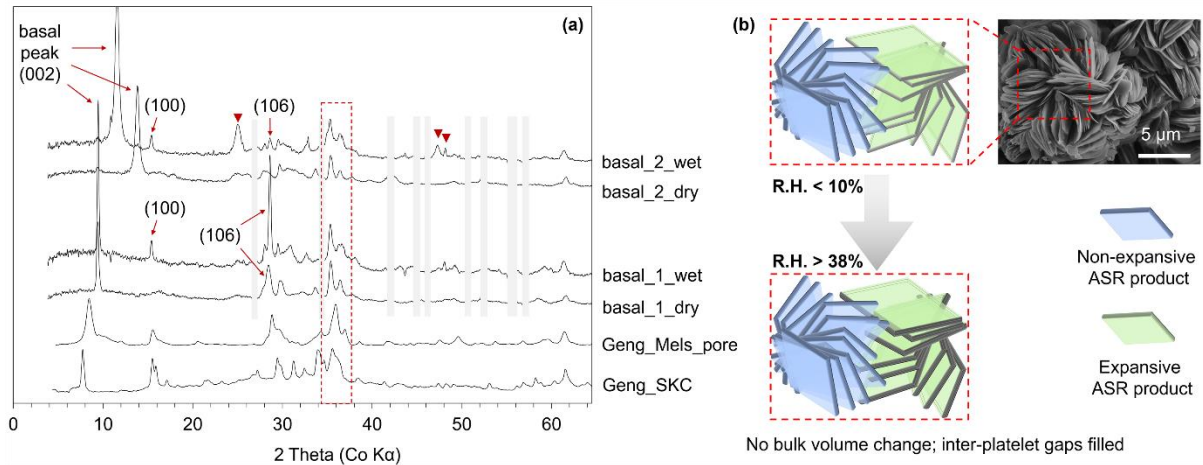
Figure 6. (a) Decoupled XRD of phase basal_1 and basal_2 in dry and wet conditions, compared with published XRD of ASR-related phases [24]. The peaks corresponding to calcite and Pt peaks are masked by grey bars for viewing convenience. (b) An illustration of the micro-process of moisture uptake by the ASR product vein. The SEM image is adopted from [28].

For both basal_1 and basal_2 phases, their XRD are comparable to the XRD of previously studied shlykovite-type products [24] in the 2theta, especially in the group of strong diffraction from 34° to 38° (red dashed square in Figure 6a). This suggests that the two phases identified here share similar layer structure as other shlykovite-type products, whereas the basal spacing of the layers are smaller here. The similarity in chemical environment is consistent with the spectroscopic study of similar products synthesized in the lab [26]. On the other hand, the thickness of each shlykovite-type layer is ~9 Å [24]. If phase basal_2 has the same layer structure, it will need to adopt an extremely tight stacking to obtain such a small basal spacing (8.89 and 7.43 Å). Particularly, in dry condition, the dendritic tips of the silicate layer will need to penetrate into the 8-unit silicate ring of the adjacent layer, to reach a basal spacing as small as 7.43 Å. Meanwhile, some diffraction peaks in basal_2_wet were not observed in other

shlykovite-type ASR products (red triangles in Figure 6a). Thus more study is needed to

provide insight into the crystal structure of the swelling phase basal_2.

So far a group of basal spacings, ranging from 7.4 Å to 13.4 Å, have been reported for the

crystalline ASR products from affected concrete. Among them, only the product with a ~8.9 Å

basal spacing (wet condition) was observed here to shrink to ~7.4 Å upon severe drying. The

basal spacings of the other products, ranging from ~10 Å to 13.5 Å, seem inert to the moisture

change. Lab-synthesis attempts indicated that their basal spacings are more determined by the

synthesis temperature [19,26]. A compression as high as 2 GPa was also proven to result in a

permanent basal spacing reduction of ~1 Å for ASR products with basal spacing around 12.2

Å from field concrete samples [31]. In a real ASR product vein, all these products may exist at

the same time, although they may have similar nano-platy morphology. It still remains largely

unclear what leads to such a variation in the stacking behavior in different ASR products.

The bulk moduli of several polymorphs of ASR products range from 27 to 76 GPa as reported

by our previous high-pressure XRD work [31], while the bulk modulus of the whole product

vein is at the scale of ~10 GPa according to indentation results [22,23,41]. This indicates a

porosity of 40% to 80% in the product vein, as roughly estimated by a Mori-Tanaka

homogenization scheme of randomly oriented thin platelets [42]. Assuming an equal volume

of phase basal_1 and basal_2, the volume ratio of basal_2 to the total product is roughly in the

range of 10% to 30%. Thus the 20% crystal structural expansion of phase basal_2 is

homogenized to a <6% volume change of the product vein, i.e. less than 2% increase on one

spatial dimension. This value is comparable to the accuracy of our experimental approach here

and therefore difficult to be established unambiguously in the present measurements.

Based on the above discussion, an illustration of the moisture-uptake in the studied ASR

product vein is given in Figure 6b. The vein contains the agglomeration of expansive (basal_2)

and non-expansive (basal_1) ASR nano-plateltes. Starting from a dry state, the expansive

product (basal_2) may uptake water into the interlayer during moisture ingress, resulting in an enlargement of basal spacing and the thickening of each platelet. However, this seems not to cause any expansion of the bulk volume of the product vein. A straightforward explanation is thus, the thickening of the nano-platelets only results in a shortening of the gaps between the platelets.

Our results suggest that the source of micro-expansive stress is not from the swelling of the crystalline ASR product during moisture ingress. The mechanism of ASR degradation thus awaits alternative explanations. A recent study showed that the early form of ASR products in nano-cracks of aggregate are often amorphous, in contrast to the nano-crystalline form when macro-expansion is already obvious [43]. It remains to be studied whether the amorphous early products may uptake water and generate swelling stress. It is also not investigated whether the recrystallization of early products is accompanied by a crystallization pressure. In the latter case, a pre-existing crack may open up due to localized crystal-growth before the whole crack/void is filled with product. This phenomenon is indeed observed in a recent study [44].

4. Conclusions

In this work, a tomographic micro-XRD measurement was applied to a freshly extracted nano-crystalline ASR product vein in varying R.H. conditions, i.e. 10% (dry), 97% (wet) and 38% (ambient). The main conclusions are summarized as follows.

1) Two nano-crystalline phases with the same morphology were found intermixed inside an ASR product vein from a damaged concrete aggregate. They exhibit distinct basal spacings – one at 10.9 Å and the other at 7.43 Å when the sample was equilibrated in R.H.=10%.

2) After the dry sample was exposed to R.H.=97% for one hour, the basal peak 7.43 Å shifted to 8.89 Å, indicating a moisture-driven enlargement of basal spacing.

372   Meanwhile the 10.9 Å peak remained unchanged. Both phases have a higher degree of

373   crystallinity in wet condition than in dry condition. Both phases remained unchanged

374   when R.H. dropped from 97% to 38%.

375   3) Despite the crystal structural expansion of one ASR product phase by uptaking water,

376   the overall ASR product vein showed no sign of clear in-situ expansion at microscale

377   of the studied sample. Therefore, the moisture ingress into nano-crystalline product

378   veins may not explain the microscale origin of the expansive stress development in

379   ASR degradation. Similar experiments are needed for more ASR product from affected

380   concrete to justify the universality of this finding.

381

382 **CRediT authorship contribution statement**

383 G. Geng: Conceptualization, Methodology, Formal analysis, Investigation, Data curation,

384 Writing - original draft. S. Barbotin, M. Shakoorioskooie and A. Leeman: Conceptualization,

385 Validation, Resources, Writing - review & editing. Z. Shi: Formal analysis, Writing - review

386 & editing. D.F. Sanchez and D. Grolimund: Methodology, Investigation, Data curation,

387 Writing - review & editing. E. Wieland and R. Dähn: Conceptualization, Methodology, Writing

388 - review & editing, Supervision, Project administration.

389

390 **Declaration of competing interest**

391 The authors declare that they have no known competing financial interests or personal

392 relationships that could have appeared to influence the work reported in this paper.

393

394 **Acknowledgement**

397   Villigen (Switzerland) was acknowledged for provision of synchrotron radiation beamtime at

398   beamline microXAS of the SLS and the Interdisciplinary Center for Electron Microscopy

399   (CIME, EPFL) for their support in the sample preparation.

400

401   **References**

402   1. P.K. Mehta, P.J.M. Monteiro, Concrete: Microstructure, Properties, and Materials, 4th ed.,

403   McGraw-Hill Companies, New York City, 2014.

404   2. W.F. Cole, C.J. Lancucki, M.J. Sandy, Products formed in an aged concrete, Cem. Concr.

405   Res. 11 (1981) 443-454.

406   3. T.E. Stanton, Influence of cement and aggregate on concrete expansion, Eng. News Record

407   1 (1940) 59-61.

408   4. B. Fournier, M.A. Bérubé, Alkali-aggregate reaction in concrete: a review of basic concepts

409   and engineering implications, Can. J. Civil Eng. 27 (2000) 167-191.

410   5. ASTM 2002 C 294-98. Standard descriptive nomenclature for constituents of natural

411   mineral aggregates. American Society for Testing and Materials, West Conshohocken, PA,

412   2002.

413   6. EN 2010 EN 932-3. Tests for general properties of aggregates—Part 3: Procedure and

414   terminology for simplified petrographic description. European Committee for

415   Standardization (CEN), Brussels, 2010.

416   7. ASTM C1293. Standard test method for determination of length change of concrete due to

417   alkali-silica reaction. American Society for Testing and Materials, West Conshohocken, PA,

418   2008.

419   8. A.E. Eskridge, J.T. Klahorst, R.E. Klingner, M.E. Kreger, Mitigation techniques for

420   structures with premature concrete deterioration due to ASR/DEF, ACI Mater. J. 106 (2009)

421   273.

422   9. J.H. Ideker, B.L. East, K.J. Folliard, M.D. Thomas, B. Fournier, The current state of the

423   accelerated concrete prism test, Cem. Concr. Res. 40 (2010) 550-555.

424   10. T. Oey, E.C. La Plante, G. Falzone, Y.H. Hsiao, A. Wada, L. Monfardini, M. Bauchy, J.W.

425   Bullard, G. Sant, Calcium nitrate: a chemical admixture to inhibit aggregate dissolution

426   and mitigate expansion caused by alkali-silica reaction, Cem. Concr. Compos. (2020)

427   103592.

428   11. M. Alnaggar, M. Liu, J. Qu, G. Cusatis, Lattice discrete particle modeling of acoustic

429   nonlinearity change in accelerated alkali silica reaction (ASR) tests, Mater. Struct. 49

430   (2016) 3523-3545.

431   12. Y. Kawabata, J.F. Seignol, R.P. Martin, F. Toutlemonde, Macroscopic chemo-mechanical

432   modeling of alkali-silica reaction of concrete under stresses, Constr. Build. Mater. 137

433   (2017) 234-245.

434   13. M. Rashidi, A. Paul, C. Do, K.E. Kurtis, The role of composition in the structure and water-

435   binding in alkali-silica reaction sol and gel, Cem. Concr. Res. 124 (2019) 105814.

436   14. A. Gholizadeh-Vayghan, F. Rajabipour, The influence of alkali–silica reaction (ASR) gel

437   composition on its hydrophilic properties and free swelling in contact with water

438   vapor, Cem. Concr. Res. 94 (2017) 49-58.

439   15. J.H.M. Visser, Fundamentals of alkali-silica gel formation and swelling: Condensation

440   under influence of dissolved salts, Cem. Concr. Res. 105 (2018) 18-30.

441   16. A. Leemann, Raman microscopy of alkali-silica reaction (ASR) products formed in

442   concrete, Cem. Concr. Res. 102 (2017) 41-47.

443   17. Z. Shi, B. Lothenbach, The combined effect of potassium, sodium and calcium on the

444   formation of alkali-silica reaction products, Cem. Concr. Res. 127 (2020) 105914.

445   18. H.F. Taylor, Cement Chemistry (Vol. 2). London: Thomas Telford, 1997.

446 19. Z. Shi, G. Geng, A. Leemann, B. Lothenbach, Synthesis, characterization, and water

447   uptake property of alkali-silica reaction products, Cem. Concr. Res. 121 (2019) 58-71.

448 20. L. De Ceukelaire, The determination of the most common crystalline alkali-silica reaction

449   product, Mater. Struct. 24 (1991) 169-171.

450 21. K. Peterson, D. Gress, T. Van Dam, L. Sutter, Crystallized alkali-silica gel in concrete

451   from the late 1890s, Cem. Concr. Res. 36 (2006) 1523-1532.

452 22. A. Leemann, P. Lura, E-modulus of the alkali–silica-reaction product determined by

453   micro-indentation, Constr. Build. Mater. 44 (2013) 221-227.

454 23. C. Hu, B.P. Gautam, D.K. Panesar, Nano-mechanical properties of alkali-silica reaction

455   (ASR) products in concrete measured by nano-indentation, Constr. Build. Mater. 158

456   (2018) 75-83.

457 24. G. Geng, Z. Shi, A. Leemann, C. Borca, T. Huthwelker, K. Glazyrin, I.V. Pekov, S.

458   Churakov, B. Lothenbach, R. Dähn, E. Wieland, Atomistic structure of alkali-silica

459   reaction products refined from X-ray diffraction and micro X-ray absorption data, Cem.

460   Concr. Res. 129 (2020) 105958.

461 25. R. Dähn, A. Arakcheeva, P. Schaub, P. Pattison, G. Chapuis, D. Grolimund, E. Wieland,

462   A. Leemann, Application of micro X-ray diffraction to investigate the reaction products

463   formed by the alkali–silica reaction in concrete structures, Cem. Concr. Res. 79 (2016) 49-

464   56.

465 26. Z. Shi, A. Leemann, D. Rentsch, B. Lothenbach, Synthesis of alkali-silica reaction product

466   structurally identical to that formed in field concrete, Mater. Design, 190 (2020) 108562.

467 27. T. Katayama, Late-expansive ASR in a 30-year old PC structure in eastern Japan,

468   Proceeding of the 14th International Conference on Alkali-Aggregate Reaction (ICAAR),

469   Austin, USA, 2012.

470   28. A. Leemann, Z. Shi, M. Wyrzykowski, F. Winnefeld, Moisture stability of crystalline

471   alkali-silica reaction products formed in concrete exposed to natural environment, Mater.

472   Des. 195 (2020) 109066.

473   29. Z. Shi, S. Park, B. Lothenbach, A. Leemann, Formation of shlykovite and ASR-P1 in

474   concrete under accelerated alkali-silica reaction at 60 and 80 °C, Cem. Concr. Res. 137

475   (2020) 106213.

476   30. A. Leemann, Z. Shi, J. Lindgård, Characterization of amorphous and crystalline ASR

477   products formed in concrete aggregates, Cem. Concr. Res. 137 (2020) 106190.

478   31. G. Geng, Z. Shi, A. Leemann, K. Glazyrin, A. Kleppe, D. Daisenberger, S. Churakov, B.

479   Lothenbach, E. Wieland, R. Dähn, Mechanical behavior and phase change of alkali-silica-

480   reaction products under hydrostatic compression, Acta Cryst. B, 76 (2020).

481   32. J. Lindgård, Ph. J. Nixon, I. Borchers, B. Schouenborg, B.J. Wigum, M. Haugen, U.

482   Åkesson, The EU "PARTNER" project - European standard tests to prevent alkali

483   reactions in aggregates: final results and recommendations, Cem. Concr. Res. 40 (2010)

484   611-635

485   33. C. N. Borca, D. Grolimund, M. Willimann, B. Meyer, K. Jefimovs, J. Vila-Comamala, C.

486   David, The microXAS beamline at the Swiss Light source: towards nano-scale imaging, J.

487   Physics: Conference Series, 186 (2009) 012003.

488   34. W. van Aarle, W.J. Palenstijn, J. Cant, E. Janssens, F. Bleichrodt, A. Dabravolski, J. De

489   Beenhouwer, K. J. Batenburg, J. Sijbers, Fast and flexible x-ray tomography using the ASTRA

490   Toolbox, Opt. Express, 24 (2016) 25129-25147.

491   35. W.J. Palenstijn, K.J. Batenburg, J. Sijbers, Performance improvements for iterative electron

492   tomography reconstruction using graphics processing units (GPUs), J. Struct. Biol. 176 (2011)

493   250-253.

494 36. D.F. Sanchez, D. Grolimund, M. Hubert, P. Bleuet, J. Laurencin, A 2D and 3D X-ray µ-
495   diffraction and µ-fluorescence study of a mixed ionic electronic conductor, Int. J. Hydrog.
496   Energy, 42 (2017) 1203-1211.

497 37. G. Ashiotis, A. Deschildre, Z. Nawaz, J.P. Wright, D. Karkoulis, F.E. Picca, J. Kieffer, The
498   fast azimuthal integration Python library: pyFAI, J. Applied Crystal. 48 (2015) 510-519.

499 38. W.S. Rasband, ImageJ, U. S. National Institutes of Health, Bethesda, Maryland, USA,
500   https://imagej.nih.gov/ij/, 1997-2018.

501 39. A. Henderson, ParaView Guide, A Parallel Visualization Application. Kitware Inc., 2007.

502 40. P. Bleuet, E. Welcomme, E. Dooryhée, J. Susini, J.L. Hodeau, P. Walter, Probing the structure
503   of heterogeneous diluted materials by diffraction tomography, Nat. Mater. 7 (2008) 468-472.

504 41. C. Zhang, L. Sorelli, B. Fournier, J. Duchesne, J. Bastien, Z. Chen, Stress-relaxation of
505   crystalline alkali-silica reaction products: Characterization by micro-and nanoindentation and
506   simplified modeling, Construct. Build. Mater.148 (2017) 455-464.

507 42. J.J. Timothy, G. Meschke, A cascade continuum micromechanics model for the effective
508   elastic properties of porous materials, Int. J. Solid. Struct. 83 (2016) 1-12.

509 43. E. Boehm-Courjault, S. Barbotin, A. Leemann, K. Scrivener, Microstructure, crystallinity and
510   composition of alkali-silica reaction products in concrete determined by transmission electron
511   microscopy, Cem. Concr. Res. 130 (2020) 105988.

512 44. A. Leemann, B. Münch, The addition of caesium to concrete with alkali-silica reaction:
513   Implications on product identification and recognition of the reaction sequence, Cem. Concr.
514   Res. 120 (2019) 27-35.